ROYAL SOCIETY
OF CHEMISTRY

PAPER

Check for updates

A comparative computational and scanning electrochemical microscopy study of factors influencing electron transfer at the hydrogenated and pristine graphite – propylene carbonate electrochemical interface†

Jason Howard,‡[ac] Dipobrato Sarbapalli, [iD] ‡[bc] Abhiroop Mishra,[bc] Nannan Shan,[cd] Garvit Agarwal,[ce] Jingjing Zhang, [iD] [ac] Michael J. Counihan,[bc] Lu Zhang, [iD] [ac] Rajeev S. Assary, [iD] *[ac] Larry A. Curtiss [iD] *[ac] and Joaquín Rodríguez-López [iD] *[bc]

Nonaqueous redox flow batteries are a promising technology that utilize redox-active species (*i.e.*, redoxmers) in solution to store energy *via* electron-transfer (ET) reactions with electrodes. However, electron transfer (ET) phenomena at the interface of graphitic electrodes and nonaqueous media are poorly understood, with several non-idealities in the use of conventional models such as the Butler–Volmer model reported. Possibilities for these non-idealities include the adsorption of redox species at the electrode, fundamental ET limitations related to the density of states at the electrode, and the presence of chemical and spatial heterogeneities at the surface of the electrode. To this point, we present a computational and experimental approach to comparatively investigate the ET behavior of two redoxmers, ferrocene (Fc) and 2,3-dimethyl-1,4-dialkoxybenzene (C7) on single layer graphene (SLG), hydrogen-functionalized SLG (H-SLG), and pristine and hydrogen-functionalized graphite electrodes. Scanning electrochemical microscopy (SECM) experiments revealed enhanced ET kinetics for both redoxmers on H-SLG electrodes compared to pristine SLG electrodes, with the degree of functionalization playing a key role in this enhancement. Electrodes such as boron-doped diamond and hydrogenated graphite mirrored these enhancements. Density functional theory (DFT) calculations indicate only small differences in the binding strengths for Fc and C7 redoxmers on SLG and H-SLG surfaces, but Marcus–Hush–Chidsey (MHC) kinetic theory analysis suggests that the density of states (DOS) of the carbon electrode likely plays a crucial role in the observed ET enhancement. These findings refine our initial assumption of binding energy (BE) as a dominant factor for interfacial behavior in the case of Fc and C7 redoxmers. Our findings create new opportunities to explore systems with varying degrees of surface modification to understand and design better redox flow batteries.

[a]*Materials Science Division, Argonne, National Laboratory, Lemont, Illinois 60439, USA. E-mail: assary@anl.gov; curtiss@anl.gov; Tel: +1-630-252-3536; +1-630-252-7380*

[b]*Department of Chemistry, University of Illinois Urbana-Champaign, 600 S Mathews Avenue, Urbana, Illinois 61801, USA. E-mail: joaquinr@illinois.edu; Tel: +1-217-300-7354*

[c]*Joint Center for Energy Storage Research (JCESR), Argonne National Laboratory, Lemont, Illinois 60439, USA*

[d]*Research Computing at Purdue University, West Lafayette, Indiana, USA*

[e]*Schrodinger Inc., New York, NY 10036, USA*

† Electronic supplementary information (ESI) available: Supporting experiments and raw experimental data. See DOI: https://doi.org/10.1039/d4ta07050j

‡ Both authors contributed equally to the article.

Introduction

Redox flow batteries (RFBs) are a promising technology for large-scale energy storage owing to their decoupled power and capacity characteristics, enabling scalability.[1,2] In RFBs, energy storage occurs between redox couples of molecules, which are stored in separate tanks and (dis)charged in a reactor separated by a membrane. Non-aqueous RFBs (NRFBs) offer additional advantages, such as accessing the higher potential window of organic solvents and the ability to engineer tailored redox-active organic molecules, oligomers, and polymers (henceforth referred to as redoxmers) for high energy density.[2] Charge storage in RFBs occurs through heterogeneous electron transfer (ET) reactions between electrodes, typically carbon electrodes, and redoxmers in solution. While the electrochemistry of

This journal is © The Royal Society of Chemistry 2025

J. Mater. Chem. A, 2025, **13**, 10097–10110 | **10097**

carbon electrodes such as graphite has been well studied in aqueous media,[3] conclusions from these studies do not necessarily apply in a straightforward manner to non-aqueous electrolyte solutions. It is known that modified graphitic surfaces have an impact on ET when used in aqueous solutions.[3–6] But to illustrate further the challenges in nonaqueous media, the presence of organic solvents at low/trace levels within aqueous solutions has been reported to lead to poor ET behavior on several graphitic electrodes such as highly-ordered pyrolytic graphite (HOPG) and glassy carbon (GC).[7–9]

These observations from the literature indicate that ET in non-aqueous solvents deserves a closer inspection of factors affecting it. One of the reasons posited to explain these observations suggest that the organic species form surface films that block ET.[3,9] Indeed, previous studies involving both experiments[10,11] and first-principles calculations[12] in our groups have indicated similar kinetic limitations to ET in propylene carbonate solvent. These have been attributed to be arising from film formation at the interface,[10] although interactions between aromatic rings in redoxmers and graphitic surfaces can also lead to distinct effects on ET depending on the structure of the adsorbing species.[10] These limitations in ET can even be observed with ubiquitous redoxmers, such as widely used ferrocene derivatives. For example, using the feedback mode of scanning electrochemical microscopy (SECM) to probe the potential dependence of ET rates showed kinetic limitations for hydroxymethylferrocene on graphene clearly occurring in non-aqueous solvents, but not in aqueous media.[11] Therefore, there is some evidence that ET can be affected by the choice of solvent. However, our studies have not yet focused on the role of carbon surface structure in influencing ET kinetics. As a result, the current study presents a combined computational and experimental efforts to investigate the role of carbon electrode surface structure on ET kinetics, within a nonaqueous solvent.

The theoretical effort in this work focuses on the binding of redoxmers to the electrode surface as this may influence adsorptive interactions and film formation. A working assumption of this study is that the binding energy (BE) is one predictive factor of whether a redoxmer forms a film.[13,14] Another factor to consider about redoxmer behavior at the surface would be intermolecular interactions.[15,16] One way to make film formation less spontaneous would be to minimize the BE of a redoxmer to the electrode by utilizing functional groups on carbon surfaces. A second possibility includes choosing redoxmers with strong repulsive molecule–molecule interactions on the electrode surface. Surface modification may also influence these intermolecular interactions. However, one must be cautious that modifying the electrode also leads to distinct changes in the electronic coupling and electronic density of states (DOS) at the Fermi level. From the Marcus–Hush–Chidsey theory[17] of heterogenous electron transfer at an electrode surface, these are all factors that can influence charge transfer.

Experimentally, we utilized reactive plasma to selectively functionalize areas of microfabricated, single-layer graphene (SLG) to be used as substrate electrodes. Specifically, we used an Ar/H$_2$ plasma for hydrogenating the graphitic carbons to sp^3

hybridized structures. We used these substrates to our advantage by applying the feedback mode of scanning electrochemical microscopy (SECM) to provide insights into redox reactivity[18,19] between modified and un-modified regions of the SLG. This comparison was done within a single experiment in which all conditions were equal when evaluating the different reactive sites on the electrode; we used propylene carbonate (PC) as representative nonaqueous solvent to minimize evaporation in the electrochemical cell. We first focus on investigating BE differences between ferrocene (Fc) and 2,3-dimethyl-1,4-dialkoxybenzene (C7) with SLG and H-SLG surfaces (see Fig. 2). Subsequently, we present experimental characterization of heterogeneous ET kinetics between these molecules and SLG/H-SLG electrodes. Furthermore, we discuss our results and attempt to explain our experimental observations with computational analysis. Finally, we explore the possibility of whether there are differences in binding and electronic states at the SLG and H-SLG surface that could be responsible for differences in experimentally measured ET kinetics.

Methods and materials

Materials

Propylene carbonate (PC, anhydrous, 99.7%), tetrabutylammonium hexafluorophosphate (TBAPF$_6$, 99%), and ferrocene (Fc, 98%) were purchased from Sigma-Aldrich. The Fc was recrystallized twice from hexane. The 2,3-dimethyl-1,4-dialkoxybenzene (referred to as 'C7' in forthcoming text) was synthesized via previously established procedures.[20,21] It should be noted that C7 belongs to a family of 1,4-dimethoxybenzene derivatives, synthesized for practical, high specific capacity RFBs.[20] Single-layer graphene (SLG) was purchased from Groll-Tex and transferred onto SiO$_2$/Si wafers using polybisphenol-A carbonate in a wet-transfer method as described in our previous work.[10,11] Boron-doped diamond (BDD) was purchased from Fraunhofer USA CMW. Graphite was synthesized using chemical vapor deposition on Ni foil as substrate, as described previously.[11]

Raman and XPS characterization

Colocalized Raman spectroscopy on the microfabricated substrates, within the SECM scan area was performed using a Nanophoton Raman instrument operating with a 532 nm laser excitation source. The Raman spectra were collected prior to SECM measurements. The laser power was limited to <0.7 mW to prevent beam damage. The Raman shift was calibrated using a neon light source within the instrument.

The XPS was performed using a Kratos Axis Ultra electron spectrometer, using monochromated Al Kα radiation (1486.6 eV). Survey spectra were recorded at energy resolution of 1 eV, pass energy 160 eV and high-resolution spectra for individual elements were recorded at 0.1 eV, pass energy 40 eV. The area interrogated was 0.3 × 0.7 mm. All spectra were calibrated to a SiO$_2$ peak at 532.8 eV,[22] and peak fitting was performed using CasaXPS v2.3.22.[23] The C=C/C–C/C–H peak was fit with an asymmetric LF function as recommended in literature.[24] GL30

10098 | J. Mater. Chem. A, 2025, 13, 10097–10110

This journal is © The Royal Society of Chemistry 2025

lineshape was used for the other functional groups. Shirley backgrounds were applied on all spectra. Functional groups within the C 1s spectrum were deconvoluted using peak assignments described in literature.[25]

Microfabrication & substrate functionalization

SLG substrates were modified to have select areas hydrogenated, leading to H-SLG and SLG regions on a single substrate using photolithography. AZ5214E photoresist was used in the positive mode for device fabrication, with AZ917 MIF developer utilized for developing UV exposed areas. Mask aligning was performed with a Karl-Suss MJB3 aligner. The complete lithography process is illustrated in Fig. S1.†

A reactive plasma with Ar/H$_2$ as source gas (5% H$_2$, 95% Ar gas mixture) was utilized to obtain H-SLG. The plasma functionalization was performed with a Tergeo plasma cleaner operating in a remote plasma mode (plasma ignited upstream in a separate chamber enabling surface functionalization over graphene etching). The recipe used 10 W power and 5 sccm Ar/H$_2$ flow. Exposure durations were varied to obtain different degrees of functionalization and are described within respective figure captions. This recipe was based on previous studies with the same instrument for obtaining H-SLG.[26,27] XPS and Raman characterization of pristine SLG and H-SLG is shown in Fig. 1. It should be noted that the XPS and Raman spectra in Fig. 1 are from H-SLG obtained by functionalizing an entire SLG substrate, unlike those used in the SECM experiments. The XPS spectrum in Fig. 1a indicates pristine SLG with little/no functional groups, highlighting that the wet transfer process does not introduce chemical impurities. H-SLG spectra in Fig. 1b shows a characteristic upshift in binding energies of the C–C/C=C peak, consistent with the literature on H-functionalized graphene.[27,28] Deconvoluting the exact extent of hydrogenation is challenging owing to the minor difference of ∼0.5 eV in between C–C and C=C binding energies.[28] Raman spectra in Fig. 1c supplements the XPS analysis with the SLG sample showing minimal defects (no D peaks observed), whereas defects induced by the Ar/H$_2$ plasma exposure are observable in the H-SLG samples. Further quantitative analysis of defect density through Raman spectroscopy is presented later in this article.

Scanning electrochemical microscopy

Scanning electrochemical microscopy (SECM) measurements were performed with a CH Instruments 920D SECM workstation, using a Wollaston wire ultramicroelectrode (UME) probe of 1.2 μm radius (Fig. S2a†) used as SECM tip. The radius of glass sheath to radius of the electrode (RG) was kept between 10–15 for all experiments through polishing. Negative feedback approach curves till 50% i_{tip}/i_∞ were used to quantify RG before experiments (Fig. S2b†). A 3 μm and 12.5 μm radius Pt UME were used for SECM analysis of BDD and graphite respectively (Fig. S3†), with RG < 5 for both electrodes. A 0.5 mm diameter Pt and 1 mm diameter Ag wire were used as counter and quasi-reference electrodes respectively. Potentials in experimental data are reported vs. the formal potential for Fc/Fc$^+$ redox couple ($E^{0\prime}$) unless otherwise mentioned. Experiments were performed
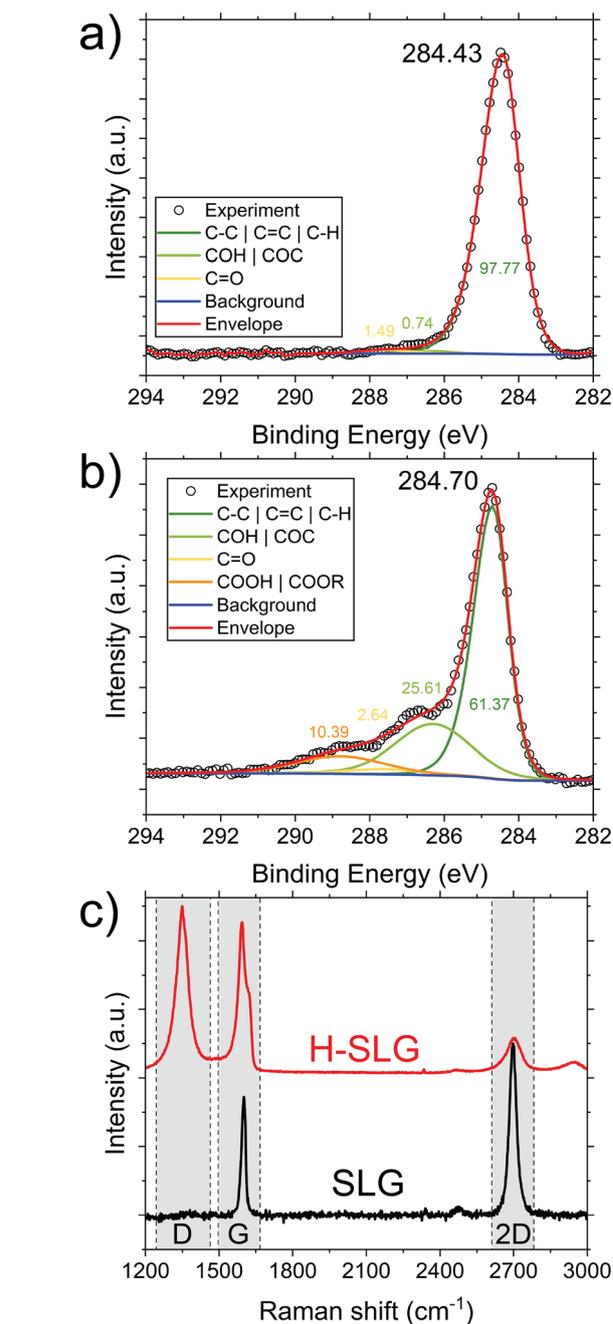

Fig. 1 Characterization of SLG samples transferred on SiO$_2$/Si wafer. XPS C 1s signals from (a) SLG, (b) H-SLG with percentage quantification from different functional groups indicated within the figures. (c) Raman spectra on the same samples with D, G and 2D peaks highlighted. Duration of Ar/H$_2$ plasma exposure for H-SLG sample was 1 min.

in a MBraun Ar-filled glovebox (O$_2$, H$_2$O < 0.1 ppm). All SECM experiments used a supporting electrolyte of 0.1 M TBAPF$_6$ in PC. The following SECM terminology is used throughout this paper: d – distance between tip and substrate, a – UME radius, L = d/a, D – diffusion coefficient of redoxmer, i_{tip} – current measured during steady state oxidation of redoxmer at SECM tip, i_∞ – mass transfer limited, steady-state current at least 50 μm away from substrate.

This journal is © The Royal Society of Chemistry 2025

J. Mater. Chem. A, 2025, 13, 10097–10110 | 10099

SECM feedback imaging and spot analysis

SECM feedback mode was used to image and extract information on electron transfer (ET) kinetics between SLG/H-SLG and select redoxmers. In feedback imaging, the redoxmer of interest (Fc or C7) was oxidized at the probe and subsequently reduced at the substrate electrode. This redox recycling near the substrate electrode is known as positive feedback; positive feedback currents above the electrodes were used to quantify heterogeneous electron transfer rate constants, k_f, using eqn (27) described in ref. 29. Diffusion coefficients used for this analysis were 3×10^{-10} m^2 s^{-1} and 2.23×10^{-10} m^2 s^{-1} for Fc and C7 respectively in propylene carbonate (PC), as measured in our previous work.[10] Positive feedback can also be obtained at open-circuit because the substrate electrode can behave like a bipolar electrode,[30,31] and k_f at open circuit represents an intrinsic ability of the electrode to engage in ET with a redoxmer.[10] A region of SiO$_2$/Si wafer (on which SLG is transferred) was always included in the scan area for feedback imaging. This enabled accurate tip positioning from the substrate by using negative feedback approach curves over the insulating SiO$_2$ surface (Fig. S2b†), as this approach curve is not sensitive to substrate electrode potential or open-circuit feedback. In all the normalized current plots, the normalized tip currents (i/i_∞) are set to vary between the positive and negative feedback limits of the SECM experimental parameters. For positioning the tip over BDD and graphite electrodes, a positive feedback approach curves was used with the substrate held at $E_{sub} - E^{0\prime}$ values of -0.4 to -0.6 V, ensuring mass transfer limitations. This enabled the use of analytical expressions for mass transfer limited positive feedback approach curves to accurately determine the tip-substrate distance (Fig. S4†).

Likewise, spot analysis with SECM was carried out following the steps described in our earlier work.[11] In brief, this approach involves holding the SECM tip at a constant potential, while the substrate electrode is biased to perform the reverse redox reaction of the tip, at different discrete potentials (in a staircase waveform). This enables correlating the k_f vs. $E_{sub} - E^{0\prime}$ experimental data with Butler–Volmer kinetics (eqn (1)) simulated using COMSOL finite element analysis:

$$k_f = k^0 \exp[-\alpha f(E - E^{0\prime})] \tag{1}$$

where, k_f is the heterogeneous rate constant for the forward reaction (from O $\rightarrow$ R), k^0 is the standard heterogeneous rate constant for the redox reaction (between O and R), α is the transfer coefficient, $E^{0\prime}$ is the formal potential, and E is the electrode potential (which we denote E_{sub} for the specific case of that applied at the substrate electrode). For redoxmers Fc and C7 with Nernstian kinetics and similar diffusion coefficients in the O and R forms, we assumed that $E_{1/2} = E^{0\prime}$; $E_{1/2}$ being the half-wave potential obtained from ultramicroelectrode (UME) voltammetry.[32] For comparison to experimental data, idealized simulations of the feedback response used $\alpha = 0.5$, which is typical for outer-sphere, heterogeneous ET reactions,[32] as well as a k^0 detailed in the corresponding figure caption. Details of the COMSOL simulation using transport of dilute species with

semi-infinite concentration boundary conditions are described in Fig. S5 and Table S1,† following our previous work.[11] COMSOL experiment parameters such as a, D, RG, and L, etc. are kept the same as corresponding experiments, as highlighted in Table S2.† Fig. S6† illustrates the estimation of feedback limits for spot analysis using eqn (27) of ref. 29. Our spot analysis measurements involve measuring tip current as a function of substrate electrode potential – all normalized tip currents vs. $E_{sub} - E^{0\prime}$ used for obtaining the results in this manuscript are presented in Fig. S7–S11.†

Computational methods

In this work the Q-Chem code[33] was used for all calculations of cluster models and binding energies. The calculations were done with the PBE[34] exchange and correlation functional along with the empirical Grimme D2 (ref. 35) correction for van der Waals interactions. All reported results were calculated with the 6-31G* basis set. Comparisons to the 6-31+G* basis set showed <0.1 eV difference in binding energy calculations. The atomic relaxations converged when gradients were below 3×10^{-4} hartree Å^{-1}, energy changes below 10^{-6} hartree, and maximum atomic displacements below 12×10^{-4} Å. In calculations of the molecular binding, the cluster/surface atoms were kept fixed. All Constrained DFT (CDFT) calculations were carried out as implemented in Q-Chem within the formalism of Wu and Van Voorhis.[36] The charge partitioning within the CDFT framework utilized Becke partitioning with the universal density[37] shift to the atomic radii or Bragg Slater shift to atomic radii for calculations including iron. Calculations including iron were limited to those for ferrocene molecules.

The VASP code was used[38–40] along with the PBE exchange and correlation functional[34] for calculations of the density of states for pristine and hydrogenated graphene. A 450 eV cutoff was used for the plane waves for all DFT calculations. A 6×6 supercell of graphene was created from a graphene unit cell. The supercells were given a 16 Å vacuum region between periodic images. One of the supercell models was populated pseudo randomly at an occupancy of 10% hydrogen to form the hydrogenated model. The hydrogenated model had its atomic positions relaxed while keeping the lattice parameters fixed using $6 \times 6 \times 1$ Monkhorst–Pack k-points mesh. Single step self-consistent field (SCF) calculations were performed with $24 \times 24 \times 1$ Monkhorst–Pack k-points mesh for the pristine and hydrogenated graphene models to determine their electronic density of states.

For calculations of binding energies with a cluster model a hexagonal shaped cluster of 216 carbon atoms with hydrogen terminations of the 36 zig zag edges was prepared to make a C$_{216}$H$_{36}$ system. Smaller clusters have been successfully used in previous studies of the binding of small organic molecules to graphene.[41] A picture of the cluster model used for BE calculations is shown in Fig. S12.†

To implement a calculation of the BE of a molecule absorbed on the surface there are effectively two schemes to consider. These are either a finite cluster calculation or a periodic repeating calculation. In this work it is shown that a cluster

10100 | J. Mater. Chem. A, 2025, 13, 10097–10110

This journal is © The Royal Society of Chemistry 2025

model can be advantageous if one can afford a large enough cluster model. While the main source of error in the cluster model comes from edge effects, the source of error in the periodic calculation comes from periodically repeating images. When the system is charged the periodic charges are particularly problematic and getting an accurate value requires a series of calculations that are fit to an appropriate form to extract the large system size limit. Studies of the adsorption of molecules on charged surfaces show that there can be large errors resulting from periodicity.[42] Because of the computational expense and tedious nature of periodic calculations, in this work cluster calculations were used.

In performing charged binding energy calculations there are ambiguities that can arise. In Section 1, of the ESI,† a thorough explanation of the ambiguities that arise in charged BE calculations and how we go about dealing with them utilizing CDFT is presented. When charge transfer occurs in the SCF calculation the standard method of computing binding/adsorption energies may not give a physically relevant result. This work aims to elaborate on these ambiguities from physical arguments based on the meaning of the BE. The main issue that arises with standard DFT is that the molecule may not take on the desired charge state. This is because one can only fix the total charge of the system within standard DFT. As a resolution to this problem the capabilities of CDFT[43] are employed to get a more physically reasonable estimate for the ambiguous values. The use of CDFT is typically related to preparing diabatic charge state for modeling charge transfer processes.[44–47] As far as we are aware, this is the first time CDFT has been used to calculate charged binding energies.

Results

Computational binding energy (BE) calculations

One key aspect of how the redoxmers interact with the electrode surface is their binding energy (BE) and associated free energy (ΔG) of adsorption. Here we focus on the BE because it is the primary component of ΔG and the most accessible for computation. In this work, we investigated the binding energies of Fc and C7 redoxmers. Calculation of the binding energies is discussed in detail under Section 1, ESI.† To interpret the BE values obtained, we chose to compare them to the BE of C7, which has been proven to form surface films during cycling.[10] Binding energies of unsolvated single molecules of Fc and C7 (in their charged and discharged state) on SLG are presented in Table 1 with the simulated structures shown in Fig. 2a and b. The negative BE results indicate that C7 tends to bind to SLG surfaces in both the charged and discharged state. This agrees with the experimental observation that C7 forms a film on SLG, although this was not observed for C7+.[10] Therefore, we considered the possibility that repulsive intermolecular interactions between the C7+ cations make the cation binding unfavorable. We did this by calculating binding energies for clusters of four neutral and four charged molecules of C7 and Fc (Fig. 2c and d).

The computational results are summarized in Table 1. The calculations with the cluster of four molecules indicate that film

Table 1 Summary of binding energies in eV per molecule for Fc/Fc$^+$, C7/C7$^+$, and PC solvent binding to single layer (SLG, Fig. S12) and hydrogenated single layer graphene (H-SLG, Fig. S16)^a

	SLG with single molecule	SLG with four molecule cluster	H-SLG with single molecule
Fc	−0.6	−0.68	−0.68
Fc$^+$	−1.44	+1.37	−0.94
C7	−1.07	−1.15	−1.19
C7$^+$	−1.66	+0.49	−1.4
PC (solvent)	−0.52	—^{a}	−0.57

^{a} No BE calculations were done for a cluster of 4 solvent molecules because the solvent molecules are neutral, and there is no charge/neutral difference to investigate, unlike the case with Fc and C7.

formation is unlikely to occur for C7$^+$ due to repulsive lateral electrostatic interactions of the charged molecules. As opposed to a single C7$^+$ molecule (with calculated BE of −1.66 eV per molecule BE with the SLG surface), the BE for the four-molecule array was +0.49 eV per molecule. The positive BE is indicative of repulsive interactions that may make the film formation with C7$^+$ redoxmer thermodynamically unfavorable. Similarly, computations of the BE per molecule for an array of four Fc$^+$ molecules produced a value of +1.37 eV per molecule as compared to a −1.44 eV for an isolated Fc$^+$ molecule. To understand the effects of hydrogen functionalization on SLG (H-SLG), we modeled a hydrogenated graphene surface by populating the central part of the graphene cluster model with a scattering of hydrogen atoms bonded to carbons, as shown in Fig. S16.† The results in Table 1 indicate that for the neutral species Fc, C7, and PC there is a slight increase in binding from SLG to H-SLG, while for the charged species Fc$^+$ and C7$^+$ there is an appreciable decrease of the BE of 0.43 eV per molecule to 0.26 eV per molecule respectively, going from SLG to H-SLG. Comparing the binding energies across Fc and C7, it appears that C7 has a stronger tendency to bind to graphitic carbons, which may be a reason to as to why we see film formation with these molecules during redox.[10] On the contrary, binding energies of Fc are close to that of the solvent PC, implying competition between Fc and the solvent for binding sites. Nevertheless, these computational calculations show differences across molecules (Fc and C7) and across electrode surfaces (SLG and H-SLG) that prompts an experimental investigation of electron-transfer behavior.

SECM analysis of Fc reactivity over SLG and H-SLG

To complement the computational BE calculations, we explore differences in ET kinetics between redoxmers on H-SLG *vs.* SLG. For the experimental work, we resorted to SECM for studying ET kinetics, since the electrochemical behavior of Fc and C7 have been reported with the same technique earlier.[10,11] These preceding measurements provide a foundation to build our understanding of how graphitic electrode structures affects redoxmer reactivity.

First, we utilized SECM using Fc as a redoxmer to map and quantify the electrochemical reactivity of pristine SLG

This journal is © The Royal Society of Chemistry 2025

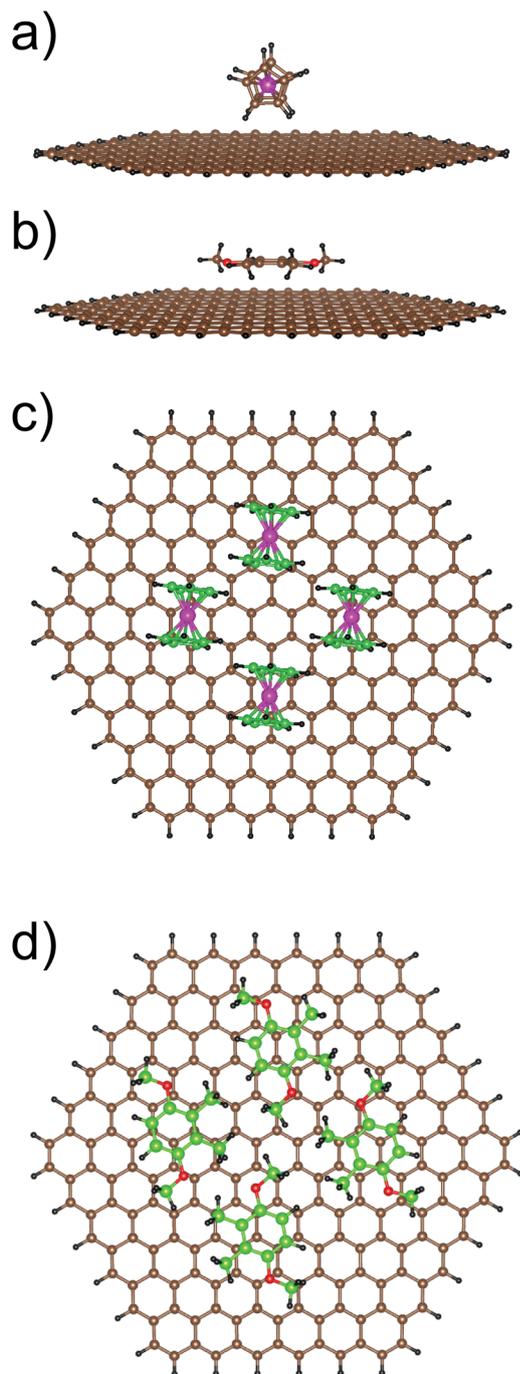*J. Mater. Chem. A*, 2025, **13**, 10097–10110 | **10101**

Fig. 2 Binding configurations of redoxmers to a pristine SLG cluster model. (a) A single Fc molecule and (b) single C7 molecule binding to the SLG surface. (c) and (d) Depict a cluster of four Fc and C7 molecules binding to the SLG surface, respectively. Color spheres: brown depicts carbon atoms in SLG, green spheres depict carbon atoms of redoxmer, black depicts hydrogen atoms, red spheres denote oxygen atoms and magenta denotes iron atoms in Fc.

Fig. 3 Electrochemical reactivity of Fc on SLG substrates, as characterized through SECM. (a) Optical micrograph of SLG substrate on SiO_2/Si wafer, after assembly inside an SECM cell with the dashed line showing the boundary between SLG and SiO_2. (b) SECM feedback imaging at different substrate potentials ($E_{sub} - E^{0\prime}$) noted within each feedback image. (c) SECM spot analysis (at location of white cross mark, bottom figure in (b)) for quantification of ET kinetic parameter α using eqn (1) applied to data between −0.4 and −0.6 V. All experiment and analysis parameters are summarized in Table S2.†

electrodes, as a baseline measurement to compare with (i) differences in electrode structure, *i.e.* H-SLG *vs.* SLG and (ii) difference in redoxmer identity, *i.e.* C7 *vs.* Fc. Fig. 3a shows the optical micrograph of SLG transferred on Si/SiO₂ wafer. SECM feedback imaging results are shown in Fig. 3b. It is evident that

the normalized currents are not reflecting mass transfer limited currents as they do not reach the theoretical maximum for i_{tip}/i_∞ at the imaging distance, indicated by the z-axis color scale. Spot analysis measurements (Fig. 3c) clearly indicate

10102 | *J. Mater. Chem. A*, 2025, **13**, 10097–10110

This journal is © The Royal Society of Chemistry 2025

a kinetically-limited ET process, with a linear fit revealing an α value of 0.25. This value is close to previously reported measurements of 0.3 in literature[48,49] and our own measurements with graphitic carbon.[11] However, α is expected to be 0.5 for an ideal, outer-sphere ET reaction such as Fc/Fc$^+$ redox. Therefore, this observation indicates anomalies with Fc$^+$ reduction at SLG. The Butler–Volmer model of electrode kinetics is derived on the basis of the transition state theory,[32] and α denotes the similarity of the transition state to the reactant or product. Given the fact that Fc $\Leftrightarrow$ Fc$^+$ redox reactions do not involve structural changes (only the Fe–C bond length changes by $\sim$0.1 Å) and any bond breakage/formation,[50] it is unlikely that the transition state would lean towards either redox state. Therefore, we expect the observed kinetic limitations in Fig. 3c to be arising out of other factors influencing local ET, that manifest as an anomalous α value.

Subsequently, we used microfabricated substrates for characterizing the differences in electrochemical behavior of Fc over SLG and H-SLG areas. Fig. 4a shows Raman D/G maps of the substrate used, with Fig. 4b clearly illustrating distinct SLG and

H-SLG areas. We performed SECM feedback experiments with reducing potentials of $E_{sub} - E^{0\prime}$ ranging between -0.15 to -0.45 V (Fig. 4c). The SECM feedback experiments revealed a stark increase in normalized feedback currents i/i_∞ over the H-SLG areas, indicating that ET kinetics over H-SLG areas were higher than those over SLG. To probe further into the differences in ET kinetics, we resolved to spot measurements with SECM, illustrated in Fig. 4d. The experimental data over H-SLG is close to what is expected from COMSOL simulations with Butler–Volmer kinetics, using $k^0 = 10^{-4}$ m s^{-1} and $\alpha = 0.5$, implying significantly faster kinetics. However, the measured k^0 values are lower than 10^{-3} m s^{-1} estimated for Fc in non-aqueous solutions using a Pt electrode.[11] On the other hand, ET kinetics between Fc and SLG on the microfabricated electrode were also slow, with mass transfer limited current (*i.e.* the positive feedback limit) attained at more negative $E_{sub} - E^{0\prime}$ values. The data for the microfabricated substrate matches well with the observations of Fc ET kinetics over pristine SLG electrodes in Fig. 3c.

Therefore, the observation of fast kinetics over H-SLG now provides evidence that the kinetic limitations can be overcome
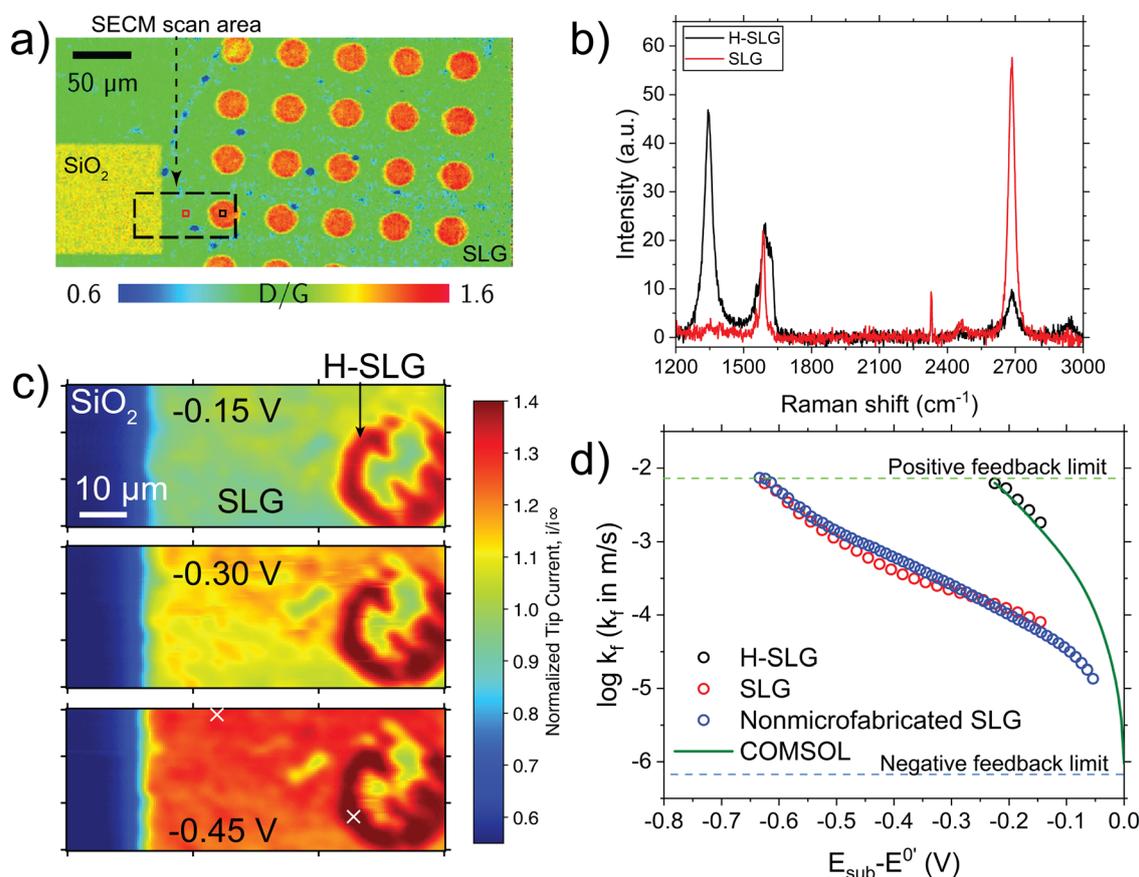

Fig. 4 Raman characterization and reactivity of Fc characterized by SECM on microfabricated SLG substrates. (a) Raman D/G map (without baseline correction) of the microfabricated sample with SECM scan area depicted in dashed rectangle; H-SLG areas were obtained with plasma exposure time of 4.5 minutes. (b) Baseline corrected Raman spectra from 10 × 10 μm square areas over H-SLG (black box in a) and SLG (red box in a). (c) SECM feedback imaging at substrate potentials $E_{sub} - E^{0\prime}$ of -0.15, -0.30 and -0.45 V. (d) ET kinetics (k_f) studied as a function of $E_{sub} - E^{0\prime}$. The location over SLG and H-SLG for the SECM spot analysis measurements are marked by white crosses within the bottom feedback image in (c). Spot analysis data from Fig. 3c (blue markers) is overlaid for comparison to non-microfabricated SLG behavior. COMSOL simulations were performed with $k^0 = 10^{-4}$ m s^{-1}, $\alpha = 0.5$, $L = 1.31$, $a = 1.2$ μm and RG = 14.1. All SECM experiment parameters are highlighted in Table S2.†

This journal is © The Royal Society of Chemistry 2025

J. Mater. Chem. A, 2025, **13**, 10097–10110 | **10103**

by modifying the electrode structure. It should be noted that our previous studies did not reveal unambiguous evidence of the Fc redox-active species adsorbing,[11] contrary to other reports.[15,51–53] Likewise, our computational BE calculations does not reveal any tendency of Fc or inactive solvent (PC) adsorbing significantly differently over the SLG and H-SLG areas. One possibility is that the SLG surface is affected by the photolithography steps, although Fig. 4d clearly shows no difference between ET kinetics of microfabricated and non-microfabricated SLG. Nevertheless, to further investigate this possibility, we conducted a control experiment wherein the plasma exposure duration was reduced (2.5 instead of 4.5 minutes) to obtain a less-defective H-SLG area (Fig. S17a and b†). The exposure to plasma should remove surface contaminations but the duration determines the degree of hydrogenation. Subsequent SECM imaging (Fig. S17c†) and spot analysis (Fig. S17d†) illustrates that ET kinetics for Fc^+ reduction is enhanced over the H-SLG area once more compared to the SLG surfaces, although to a lesser degree than in Fig. 4d. Fig. S18† confirms the lower defect density in the H-SLG obtained with 2.5 minutes of exposure. Therefore, the enhancement in ET kinetics is clearly linked to the degree of hydrogenation of the surface.

The observation of increased ET kinetics over functionalized SLG has been reported in literature, with hydroxymethyl ferrocene reactivity (in aqueous solution) over Ar-plasma induced defects increasing compared to defect-free SLG.[54] This study reported that k^0 increases as a function of defect density owing to an enhancement in density of states (DOS). However, after a certain degree, it decreases rapidly owing to decreased conductivity of the electrode. To compare our results with their report, we quantified the defect density using Raman data from Fig. S18.† The intensity ratios were used to compute L_d (mean distance between defects) in H-SLG following eqn (2) (as described in ref. 54):

$$\frac{I_D}{I_G} = C_A \frac{(r_a^2 - r_s^2)}{(r_a^2 - 2r_s^2)} \left[e^{-\pi r_s^2/L_D^2} - e^{-\pi(r_a^2 - r_s^2)/L_D^2} \right] \quad (2)$$

where, $C_A = 4.2$, $r_s = 1$ nm and $r_a = 3.1$ nm and represent electron-phonon elements, and radii of structurally disordered and activated radii respectively.[54,55]

L_d for the samples with 2.5 and 4.5 minutes exposure time was estimated to be 11.23 and 1.97 nm respectively. These estimates enable a qualitative comparison of our results to the findings in ref. 54, which found that their highest k^0 measurement occurred at an L_D value of ~2 nm while little to no change in k^0 was observed at higher L_D values. Although there are a few differences in our methodologies (explained in the ESI Section 2†), there is some degree of agreement in the sense that the presence of defects on carbon electrodes leads to faster ET kinetics, as we observe for the 4.5 minutes modification. However, we also observe kinetic enhancements even when L_D ~11.23 for the 2.5 min-modified sample. Thus, our results indicate that H-functionalization affects the dependence of k_f as a function of $E_{sub} - E^{0'}$ in non-aqueous media. This also suggests that there might be differences in the behavior of

defects in aqueous and non-aqueous media, and findings from one system do not necessarily translate to the other.

SECM analysis of C7 reactivity over SLG and H-SLG

After characterizing the electrochemical behavior of chemically stable Fc redoxmers across SLG and H-SLG, we further investigated the C7 redoxmer. Previous work has illustrated C7 to undergo chemical decomposition pathways[20,56] potentially leading to interfacial processes such as film formation.[10] For investigating the reactivity of C7, we reutilized the substrate used in the investigation for Fc. SECM feedback imaging illustrated that ET kinetics were close to mass transfer limits when the substrate was left at open circuit at its equilibrium potential (*i.e.*, OCP conditions). However, the application of substrate potential corresponding to $E_{sub} - E^{0'}$ of −0.15 V led to decreased feedback currents, implying decreased ET kinetics associated with $C7^+$ reduction over SLG areas, as shown in Fig. 5a. Faster kinetics were observed over H-SLG areas, similar to what we observed with Fc as redoxmer. Further quantitative analysis of k_f distribution over SLG and H-SLG electrodes in Fig. 5b, before and after cycling the redoxmer (Fig. S19†) yielded some insight. Over the SLG areas before cycling, there is a clear decrease in ET kinetics from OCP to biased condition ($E_{sub} - E^{0'}$ of −0.15 V). After 50 cycles, the OCP kinetics remain low, and possess a similar distribution as of the biased condition. This reduction in OCP kinetics after cycling is not seen over the H-SLG areas, implying that in the case of C7, the H-SLG is more effective in preventing the inhibition of ET kinetics at low $E_{sub} - E^{0'}$ values. We also performed the spot analysis for quantifying k_f over a wider range of substrate potentials, as shown in Fig. 5c. As observed, the spot analysis corroborates our previous conclusion that k_f values over H-SLG are higher at less negative $E_{sub} - E^{0'}$ values. However, positive feedback limit k_f values are still attained at $E_{sub} - E^{0'} < -0.75$ V, for both SLG and H-SLG electrode areas. Such conditions imply artificially low α values, and therefore, indicate that there might be additional mechanisms limiting $C7^+$ reduction rates at SLG/H-SLG electrodes, following the discussion of anomalous α values observed for Fc^+ reduction with SLG electrodes. In summary, H-SLG helps alleviate some of the kinetic limitations observed for the $C7^+$ reduction, especially in the low overpotential region, but only to a limited degree.

Comparison to the SECM feedback response over bulk electrodes with sp³ surfaces: boron-doped diamond and hydrogenated graphite

To explore whether bulk electrode materials with sp³ hybridized surfaces could lead to higher rates of ET, we resorted to measurements with boron-doped diamond (BDD) and Ar/H$_2$ plasma-functionalized graphite. Beginning with BDD, profilometry shown in Fig. 6a revealed the height of surface features varying on the order of ±0.5 μm. Raman spectrum of BDD (Fig. 6b) indicated presence of electronically conducting sp² carbon at 1520 cm⁻¹.[57] The peak at 1215 cm⁻¹ indicates significant boron doping to ensure conductivity.[57–59] The sharp peak at 1325 cm⁻¹ originates from sp³ carbon associated with
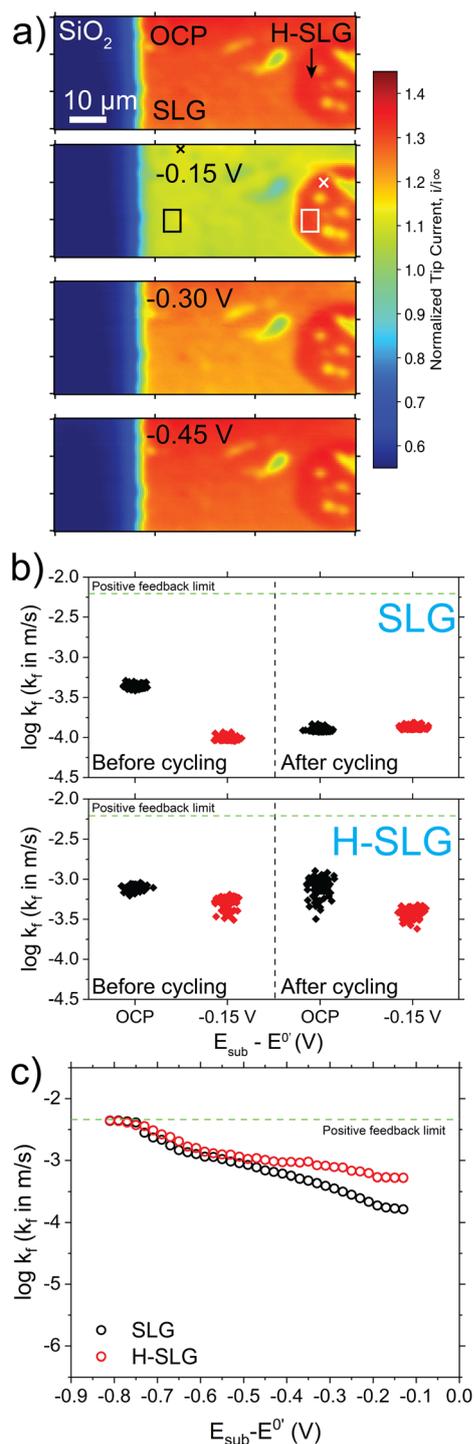
Fig. 5   Reactivity of C7 over SLG and H-SLG as characterized by SECM. (a) SECM mapping of electrochemical reactivity at open circuit and at substrate $E_{sub} - E^{0'}$ of −0.15 V, −0.30 V and −0.45 V before cycling of C7 at the substrate (Fig. S19†). (b) Distribution of rate constants from SLG and H-SLG areas, before and after cycling C7 with the substrate. (c) SECM spot analysis between SLG and H-SLG regions. Rate constant distributions were obtained from 27 μm² areas, denoted by white and black rectangles within negative feedback image of −0.15 V in (a). Spot analysis was obtained from spots indicated by white and black crosses within the SECM feedback image of −0.15 V in (a). All experiment parameters are summarized in Table S2.†
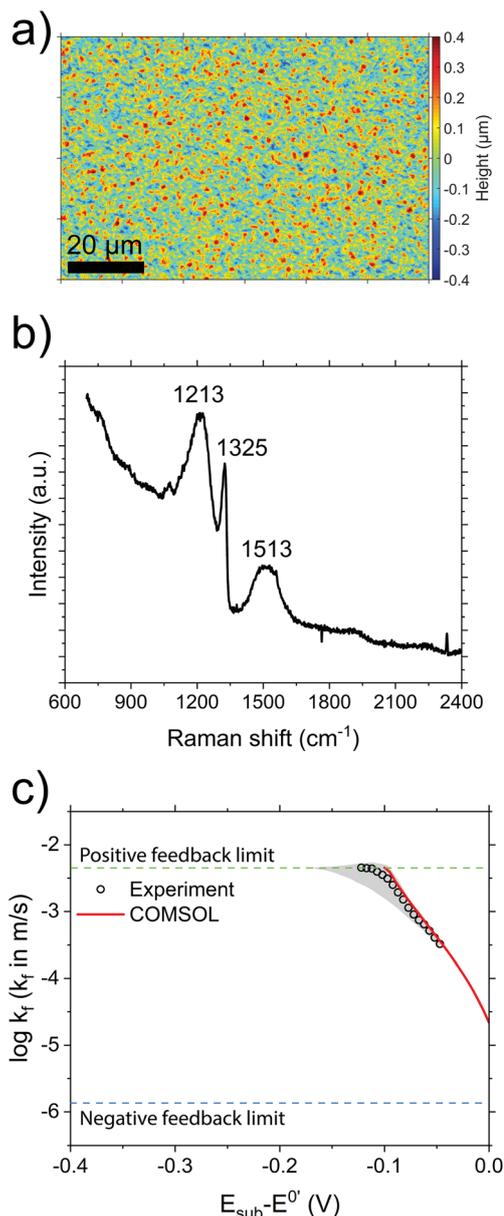
Fig. 6   Reactivity of Fc over BDD electrodes. (a) 2D profilometry of the sample, illustrating roughness varying over ±0.5 μm. (b) Raman spectra of BDD with 532 nm excitation wavelength. (c) Spot analysis of Fc over BDD. COMSOL simulations were performed with $k^0 = 10^{-2}$ m s^{-1}, $\alpha = 0.5$, $L = 0.787$, $a = 3$ μm and RG = 4.4. Standard deviation from 3 experiments is shown with the shaded area. The experimental data is the data from a single experiment, and not the average data. All experimental parameters are summarized in Table S2.†

diamond.[57] Spot analysis of Fc reveals fast kinetics (Fig. 6c), similar to those observed over H-SLG in Fig. 4d, and consistent with COMSOL simulations with $\alpha = 0.5$. This observation agrees with our expectation that materials with sp³ hybridized surfaces can mitigate kinetic limitations associated with the reduction of Fc⁺ to Fc.

Likewise, we explored hydrogen plasma functionalized graphite (H-graphite) samples, from the same batch of material grown for our previous study[11] obtained by chemical vapor

This journal is © The Royal Society of Chemistry 2025

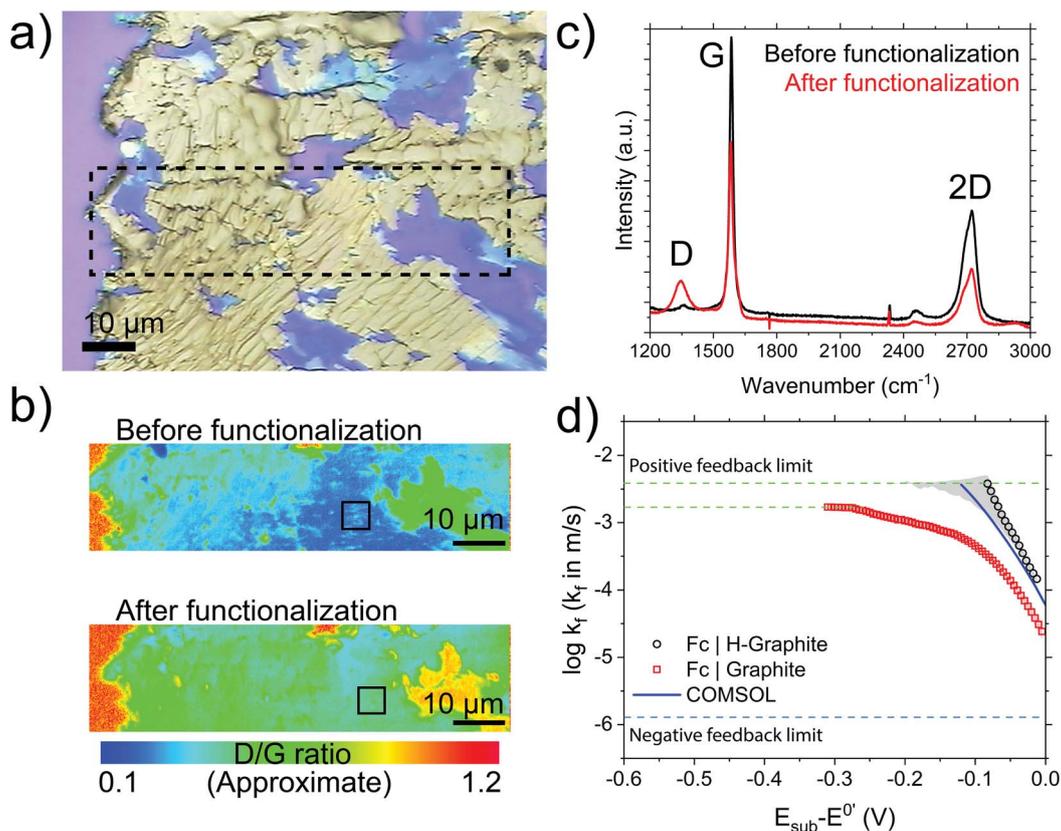*J. Mater. Chem. A*, 2025, **13**, 10097–10110 | **10105**

Fig. 7 Reactivity of Fc with H-graphite electrodes. (a) Optical micrograph of the graphite substrate on Si wafer. (b) Raman 2D/G maps (without baseline subtraction) illustrating spatial changes in the Raman signature of graphite after functionalization with Ar/H_2 plasma. (c) Raman spectra illustrating the increased D peak intensity. (d) Experimental data from SECM spot analysis using Fc redoxmer in solution (with standard deviation from 3 measurements shown in shaded area, experimental data denoting data from a single experiment, and not the average). Data from Fc reactivity on graphite from our previous work is overlaid in the same figure, along with results from COMSOL simulation (in blue) with $k^0 = 10^{-3}$ m s^{-1}, $\alpha = 0.5$, $L = 0.24$ and RG = 2.70, $a = 12.5$ μm. Note, the difference in positive feedback limit from the two datasets arise due to different tip–substrate distances involved with the SECM experiment. H-graphite was obtained with plasma exposure duration was 3.5 minutes, under a power of 20 W and gas flow rate of 4 sccm. 2D/G maps in (b) are from the region denoted by the dashed box in (a). Raman spectra in (c) was obtained by averaging over 5 × 5 μm areas within the black boxes in (b). All SECM experiment parameters are summarized in Table S2.†

deposition. The graphite was transferred on Si/SiO$_2$ wafer (Fig. 7a) through a wet transfer process without any sacrificial polymer coating on the surface. Raman analysis before and after functionalization confirmed changes in the graphite structure, with D peak intensities becoming more prominent (Fig. 7b and c). SECM spot analysis using Fc as a redoxmer (Fig. 7d) revealed faster ET kinetics than compared with pristine graphite electrodes measured previously.[11] Likewise, the spot analysis data from the H-graphite electrode is similar to theoretical COMSOL result generated from Butler–Volmer kinetics. Therefore, surface functionalization of the bulk graphite substrate was observed to enable fast Fc ET behavior, whereas the pristine graphite exhibited kinetically limited ET behavior.[11] This experiment serves as further evidence of surface functionalization being key in overcoming kinetically-limiting ET behavior of redoxmers in non-aqueous media.

Computational insights in the context of the MHC formalism

From computations, only a small BE difference (0.1 to 0.5 eV per molecule) is found for the SLG and H-SLG models for both Fc/

Fc$^+$ and C7/C7$^+$ (Table 1). Experimentally, we investigated the reduction of the two redoxmers. Therefore, we expect the binding energies in the neutral state to be more important because the molecules need to get off the surface and allow for new charged molecules to get to the surface and undergo reduction. However, in the neutral reduced state, the difference is on the low end of ∼0.1 eV, indicating that in both SLG and H-SLG, there should be little/no difference in the kinetics of the reduction reaction owing to binding. Likewise, even if we consider the greater difference in binding in the charged state, our four-molecule cluster calculations indicated that intermolecular repulsion makes binding thermodynamically unfeasible for a cluster of redoxmer molecules in solution. This leads to the question of why the ET kinetics vary between SLG and H-SLG, especially in the case of Fc/Fc$^+$ where effects like film formation are not expected. Some other factors that could contribute are electronic coupling, density of states (DOS), and reorganization energy. The reorganization energy would be dominated by solvent-redoxmer effects, which are constant across experiments in this work. Thus, we do not expect this to be an

10106 | *J. Mater. Chem. A*, 2025, **13**, 10097–10110

This journal is © The Royal Society of Chemistry 2025

appreciable factor in causing differences in the rate constants for SLG and H-SLG. On the other hand, it was found from the 10% occupied hydrogenated graphene model that there was an enhancement of the DOS near the Fermi level. From the Marcus–Hush–Chidsey theory[17,60,61] of heterogenous electron transfer at electrode interfaces, enhancing the DOS of the electrode around the Fermi level should produce a higher rate constant. Eqn (3) gives the form of the Marcus–Hush–Chidsey theory for electron transfer at an electrode surface for the forward reduction reaction:

$$k_{\text{red}} = \frac{2\pi}{\hbar\sqrt{4\pi\lambda k_B T}} \int_{-\infty}^{\infty} \exp\left(-\frac{(\varepsilon - \lambda - e\eta)^2}{4\lambda k_B T}\right) \rho(\varepsilon)f(\varepsilon)|H_{k_A}(\varepsilon)|^2 d\varepsilon$$

(3)

In eqn (3), λ is the reorganization energy, ε is the energy of an electron in the electrode referenced to the Fermi level, $\rho(\varepsilon)$ is the density of electronic states, $f(\varepsilon)$ is the Fermi–Dirac distribution electron occupation of available states in the electrode, $|H_{k_A}(\varepsilon)|^2$ is the electronic coupling between an electronic state wave vector k in the electrode with the acceptor molecule averaged over all wave vectors with a given energy ε,[62] e is the fundamental unit of charge, and η is the overpotential.

Here it is assumed the reorganization energy and coupling are independent of the overpotential. While the units of eqn (3) are in s^{-1} it should be related to the heterogenous rate constant (k_f) in m s^{-1} by a proportionality factor.[32] The DOS for SLG is shown in Fig. 8a while the DOS for the H-SLG model is shown in Fig. 8b along with a magnified image close to the Fermi level in Fig. 8c. The results of these DOS calculations show an enhancement of the DOS in the vicinity of the Fermi level for the H-SLG as compared to SLG. Based on eqn (3) if the reorganization energy and coupling parameters were constant, the increased DOS would lead to an enhancement in the ET kinetics. In the work of ref. 54 it was also found that defects on graphene could enhance the DOS at the Fermi level and it was concluded to be a factor in enhancement of heterogenous rate constants.[61,62] A common approximation is to assume the coupling is constant and taking it out of the integral and then eqn (3) can be evaluated up to a constant factor to determine what effect just the DOS would have on the rate constant. Integrations using the H-SLG and SLG DOS (while fixing the other parameters) with a reorganization energy of 0.5 eV suggest an increase in the rate constant of about 2 orders of magnitude for H-SLG in the range of 0 V to −0.6 V overpotential. The
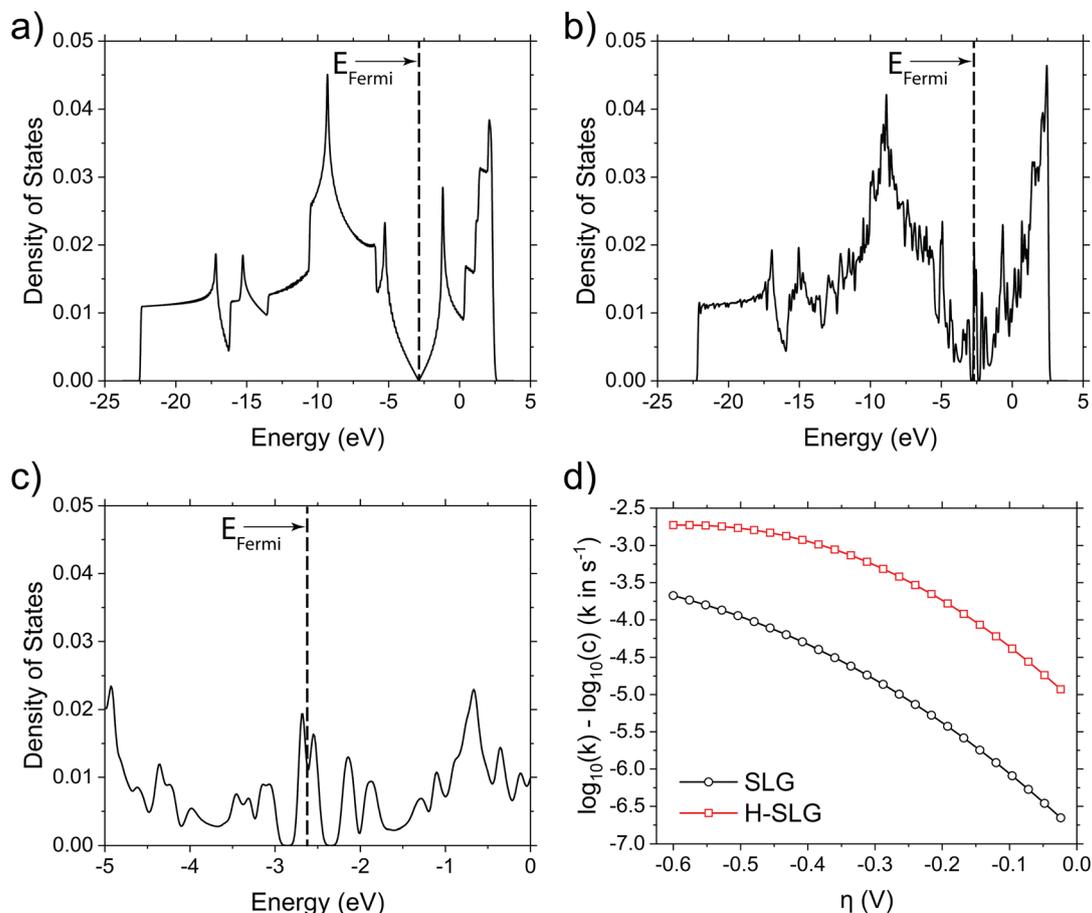

Fig. 8 Computational analysis of DOS for selected surfaces and their effects. (a) Density of states for SLG. (b) Density of states for 10% occupied model of H-SLG. (c) Zoom in of (b) around the Fermi energy. (d) Relative rate constants for H-SLG and SLG up to an unknown constant c calculated by integrating eqn (3) with the DOS from (a) and (b) while assuming the electronic coupling was a constant factor brought out of the integral and equivalent for H-SLG and SLG. In (d), eqn (3) was evaluated at 300 K and with a reorganization energy of 0.5 eV.

This journal is © The Royal Society of Chemistry 2025

J. Mater. Chem. A, 2025, **13**, 10097–10110 | **10107**

explicit comparison of these integrations is shown in Fig. 8d, and these results qualitatively match the trends seen in Fig. S17d.† We expect this trend to hold for bulk graphitic carbons as well since the DOS of graphite and graphene are similar, which also explains our observation of faster ET kinetics observed for Fc over hydrogenated graphite and most likely, BDD. Despite this increase in rate constant, it is still possible that other issues such as redoxmer film formation may obscure such effects, which may account for the lower reactivity observed for C7 in Fig. 5.

Unfortunately, evaluating the electronic coupling term in eqn (3) is complicated. In principle the electronic coupling needs to be sampled as a canonical average over configurations near the transition state and it is possible the electronic coupling could fluctuate substantially over time.[63] This makes results from single point configurations of electronic coupling unreliable. Also, the method for computing electronic coupling with CDFT in Q-Chem is not representative of the wave vector by wave vector coupling calculation prescribed by Marcus[62] needed to evaluate the integral in eqn (3). Electronic coupling calculations implemented in Q-Chem and other DFT based codes are based on computation using an overlap of wave functions approximated by a Slater determinant of the DFT orbitals[43] and do not afford the ability to determine couplings as prescribed in eqn (3).

Predictions for future work

With the insight provided by the experiments and computational above, we thought it would be useful to screen other redoxmers which might be of interest for future experiments. We report the binding energies from a collection of redoxmers (Section 3, ESI†), with their ChemDraw structures shown in Fig. S20.† All the molecules are catholyte molecules (including cyclopropeniums and alkoxybenzenes) except for benzothiadiazole derivatives **5a** and **5b**, which are anolytes. Of particular interest are molecules **1b** (an asymmetric cyclopropenium) and **5a** (benzothiadiazole). **1b** and **5a** are a catholyte[64] and anolyte[65] molecule respectively, both of which possess desirable characteristics of a practical RFB molecule: high potentials (E^0 of 0.8 V and -1.9 V $vs.$ Fc/Fc$^+$), high solubility (>0.5 M) and stability during RFB cycling. Therefore, the BE computation may impact development of redox-active molecules for RFBs and are presented in Tables S3–S6.† Interestingly, we note that molecules like **1b**, which have redox states of +1 and +2 show binding energies more negative than Fc and C7, indicating a greater preference of binding with graphitic carbon. On the other hand, anolyte molecule **5a** shows binding energies lower than Fc and PC solvent, with constrained DFT calculations showing a BE of -0.25 eV in the -1 state. These results indicated that positively charged species may tend to exhibit stronger binding towards sp^2 hybridized graphitic carbon surfaces containing delocalized π-electrons. ET behavior of these molecules could be interesting given some of these molecules have much higher and lower binding energies than the Fc and C7 molecules investigated herein, and therefore merits further study in future works.

Conclusions

In this work, we started off by hypothesizing that the BE of redoxmers to graphitic carbon surfaces may be a determining factor in film formation, as we had observed previously for 2,3-dimethyl-1,4-dialkoxybenzene (C7) on multi-layer graphene. However, BE calculations of both Fc and C7 redoxmers had negligible differences (0.1 to 0.5 eV per molecule) between SLG and H-SLG electrodes, despite in all cases showing clear differences in SECM feedback experiments. Specifically, SECM imaging and spot-analysis over H-SLG surfaces showed that ET kinetics are significantly enhanced, with the degree of functionalization being a key factor in this enhancement. In the case of Fc, k_f values increased by an order of magnitude at $E_{sub} - E^{0\prime}$ of -0.15 V, along with the observation of Nernstian ET behavior over H-SLG. Upon comparison to literature, we found subtle differences in how the defects affect ET kinetics. Previous work showed that the defects affect k^0 of the ET reactions, whereas our study highlighted also that the measured potential region ($E_{sub} - E^{0\prime}$) is determining as well. Apart from BE, MHC kinetic theory highlighted other possible factors that explained our observation of faster kinetics over H-SLG. In this regard, we investigated the electrode DOS and observed that ET kinetics theoretically calculated using the MHC model and DOS from defect and defect-free electrodes qualitatively suggest similar trends to those observed experimentally. While the factor of electronic coupling could not be ruled out, it is likely that the change in DOS due to plasma functionalization does play a role in the enhancement of ET kinetics observed over H-SLG. Consequently, these explanations help us refine our hypothesis that the BE is a controlling factor of interfacial behavior in the case of Fc and C7 redoxmers. This refinement is necessary, as ET kinetics for the C7 system remained significantly lower than for Fc, suggesting that film formation could still play a role. However, our results indicate that electronic structure factors on the electrode are likely dominant. These findings create new pathways to design electrodes for NRFBs and help us make predictions of redoxmers that could be studied in the future to further explore reactive trends. Specifically, we expect device-level investigation into the role of surface functionality and related processes to engineer the same (such as thermal, chemical, plasma treatments) being an important direction to pursue in efforts to manipulate electrode performance in RFBs. Additionally, this work provides fundamental insight into non-aqueous electrochemical technologies based on organic redox mediators, which may include electrosynthesis and electrochemical carbon capture among others.

Data availability

The data supporting this article have been included as part of the ESI.†

Author contributions

J. H. and D. S. – conceptualization, formal analysis, investigation, methodology, writing – original draft. A. M. – investigation,

10108 | *J. Mater. Chem. A*, 2025, **13**, 10097–10110

This journal is © The Royal Society of Chemistry 2025

Conflicts of interest

There are no conflicts to declare.

Acknowledgements

References

1 L. Trahey, F. R. Brushett, N. P. Balsara, G. Ceder, L. Cheng, Y.-M. Chiang, N. T. Hahn, B. J. Ingram, S. D. Minteer, J. S. Moore, K. T. Mueller, L. F. Nazar, K. A. Persson, D. J. Siegel, K. Xu, K. R. Zavadil, V. Srinivasan and G. W. Crabtree, *Proc. Natl. Acad. Sci. U. S. A.*, 2020, **117**, 12550–12557.

2 J. Luo, B. Hu, M. Hu, Y. Zhao and T. L. Liu, *ACS Energy Lett.*, 2019, **4**, 2220–2240.

3 R. L. McCreery, *Chem. Rev.*, 2008, **108**, 2646–2687.

4 Y. Li, R. Jarosova, M. E. Weese-Myers and A. E. Ross, *Anal. Chem.*, 2022, **94**, 4803–4812.

5 M. Hersey, S. N. Berger, J. Holmes, A. West and P. Hashemi, *Anal. Chem.*, 2019, **91**, 27–43.

6 K. J. Kim, M.-S. Park, Y.-J. Kim, J. H. Kim, S. X. Dou and M. Skyllas-Kazacos, *J. Mater. Chem. A*, 2015, **3**, 16913–16933.

7 Y. Liu and M. S. Freund, *Langmuir*, 2000, **16**, 283–286.

8 G. Zhang, P. M. Kirkman, A. N. Patel, A. S. Cuharuc, K. McKelvey and P. R. Unwin, *J. Am. Chem. Soc.*, 2014, **136**, 11444–11451.

9 L. Xiong, C. Batchelor-McAuley, K. R. Ward, C. Downing, R. S. Hartshorne, N. S. Lawrence and R. G. Compton, *J. Electroanal. Chem.*, 2011, **661**, 144–149.

10 T. S. Watkins, D. Sarbapalli, M. J. Counihan, A. S. Danis, J. Zhang, L. Zhang, K. R. Zavadil and J. Rodríguez-López, *J. Mater. Chem. A*, 2020, **8**, 15734–15745.

11 R. Gaddam, D. Sarbapalli, J. Howard, L. A. Curtiss, R. S. Assary and J. Rodríguez-López, *Chem.–Asian J.*, 2023, **18**, e202201120.

12 J. D. Howard, R. S. Assary and L. A. Curtiss, *J. Phys. Chem. C*, 2020, **124**, 2799–2805.

13 J. Hui, S. Pakhira, R. Bhargava, Z. J. Barton, X. Zhou, A. J. Chinderle, J. L. Mendoza-Cortes and J. Rodríguez-López, *ACS Nano*, 2018, **12**, 2980–2990.

14 J. A. Mann, J. Rodríguez-López, H. D. Abruña and W. R. Dichtel, *J. Am. Chem. Soc.*, 2011, **133**, 17614–17617.

15 N. Kurapati, P. Pathirathna, C. J. Ziegler and S. Amemiya, *ChemElectroChem*, 2019, **6**, 5651–5660.

16 S. Li, J. Li, H. Yu, S. Pudar, B. Li, J. Rodríguez-López, J. S. Moore and C. M. Schroeder, *J. Electroanal. Chem.*, 2020, **875**, 114070.

17 Y. Zeng, R. B. Smith, P. Bai and M. Z. Bazant, *J. Electroanal. Chem.*, 2014, **735**, 77–83.

18 D. Sarbapalli, A. Mishra, K. O. Hatfield, Z. T. Gossage and J. Rodríguez-López, Scanning electrochemical microscopy; a versatile tool for inspecting the reactivity of battery electrodes, in *Batteries: Materials principles and characterization methods*, ed. C. Liao, IOP in Renewable and Sustainable Power, 2021, ch. 9, pp. 9-1–9-44, DOI: 10.1088/978-0-7503-2682-7ch9.

19 A. Mishra, D. Sarbapalli, O. Rodríguez and J. Rodríguez-López, *Annu. Rev. Anal. Chem.*, 2023, **16**, 93–115.

20 J. Huang, B. Pan, W. Duan, X. Wei, R. S. Assary, L. Su, F. R. Brushett, L. Cheng, C. Liao, M. S. Ferrandon, W. Wang, Z. Zhang, A. K. Burrell, L. A. Curtiss, I. A. Shkrob, J. S. Moore and L. Zhang, *Sci. Rep.*, 2016, **6**, 32102.

21 J. Huang, L. Su, J. A. Kowalski, J. L. Barton, M. Ferrandon, A. K. Burrell, F. R. Brushett and L. Zhang, *J. Mater. Chem. A*, 2015, **3**, 14971–14976.

22 D. S. Jensen, S. S. Kanyal, N. Madaan, M. A. Vail, A. E. Dadson, M. H. Engelhard and M. R. Linford, *Surf. Sci. Spectra*, 2013, **20**, 36–42.

23 N. Fairley, V. Fernandez, M. Richard-Plouet, C. Guillot-Deudon, J. Walton, E. Smith, D. Flahaut, M. Greiner, M. Biesinger, S. Tougaard, D. Morgan and J. Baltrusaitis, *Appl. Surf. Sci. Adv.*, 2021, **5**, 100112.

24 G. S. Major, D. Shah, T. G. Avval, V. Fernandez, N. Fairley and M. R. Linford, *Vacuum Technology & Coating*, 2020, 35–39.

25 R. I. R. Blyth, H. Buqa, F. P. Netzer, M. G. Ramsey, J. O. Besenhard, P. Golob and M. Winter, *Appl. Surf. Sci.*, 2000, **167**, 99–106.

26 H. Ryu, D.-H. Kim, J. Kwon, S. K. Park, W. Lee, H. Seo, K. Watanabe, T. Taniguchi, S. Kim, A. M. van der Zande, J. Son and G.-H. Lee, *Adv. Electron. Mater.*, 2022, **8**, 2101370.

27 J. Son, N. Buzov, S. Chen, D. Sung, H. Ryu, J. Kwon, S. Kim, S. Namiki, J. Xu, S. Hong, K. Watanabe, T. Taniguchi, W. P. King, G.-H. Lee and A. M. van der Zande, *Adv. Mater.*, 2019, **31**, 1903424.

28 M. Pumera and C. H. A. Wong, *Chem. Soc. Rev.*, 2013, **42**, 5987–5995.

29 C. Lefrou and R. Cornut, *ChemPhysChem*, 2010, **11**, 547–556.

This journal is © The Royal Society of Chemistry 2025

J. Mater. Chem. A, 2025, **13**, 10097–10110 | 10109

30 H. Xiong, J. Guo and S. Amemiya, *Anal. Chem.*, 2007, **79**, 2735–2744.

31 A. I. Oleinick, D. Battistel, S. Daniele, I. Svir and C. Amatore, *Anal. Chem.*, 2011, **83**, 4887–4893.

32 J. Bard Allen and R. Faulkner Larry, *Electrochemical Methods: Fundamentals and Applications*, John Wiley & Sons, New York, 2nd edn, 2001.

33 Y. Shao, Z. Gan, E. Epifanovsky, A. T. B. Gilbert, M. Wormit, J. Kussmann, A. W. Lange, A. Behn, J. Deng, X. Feng, D. Ghosh, M. Goldey, P. R. Horn, L. D. Jacobson, I. Kaliman, R. Z. Khaliullin, T. Kuś, A. Landau, J. Liu, E. I. Proynov, Y. M. Rhee, R. M. Richard, M. A. Rohrdanz, R. P. Steele, E. J. Sundstrom, H. L. Woodcock, P. M. Zimmerman, D. Zuev, B. Albrecht, E. Alguire, B. Austin, G. J. O. Beran, Y. A. Bernard, E. Berquist, K. Brandhorst, K. B. Bravaya, S. T. Brown, D. Casanova, C.-M. Chang, Y. Chen, S. H. Chien, K. D. Closser, D. L. Crittenden, M. Diedenhofen, R. A. DiStasio, H. Do, A. D. Dutoi, R. G. Edgar, S. Fatehi, L. Fusti-Molnar, A. Ghysels, A. Golubeva-Zadorozhnaya, J. Gomes, M. W. D. Hanson-Heine, P. H. P. Harbach, A. W. Hauser, E. G. Hohenstein, Z. C. Holden, T.-C. Jagau, H. Ji, B. Kaduk, K. Khistyaev, J. Kim, J. Kim, R. A. King, P. Klunzinger, D. Kosenkov, T. Kowalczyk, C. M. Krauter, K. U. Lao, A. D. Laurent, K. V. Lawler, S. V. Levchenko, C. Y. Lin, F. Liu, E. Livshits, R. C. Lochan, A. Luenser, P. Manohar, S. F. Manzer, S.-P. Mao, N. Mardirossian, A. V. Marenich, S. A. Maurer, N. J. Mayhall, E. Neuscamman, C. M. Oana, R. Olivares-Amaya, D. P. O'Neill, J. A. Parkhill, T. M. Perrine, R. Peverati, A. Prociuk, D. R. Rehn, E. Rosta, N. J. Russ, S. M. Sharada, S. Sharma, D. W. Small, A. Sodt, T. Stein, D. Stück, Y.-C. Su, A. J. W. Thom, T. Tsuchimochi, V. Vanovschi, L. Vogt, O. Vydrov, T. Wang, M. A. Watson, J. Wenzel, A. White, C. F. Williams, J. Yang, S. Yeganeh, S. R. Yost, Z.-Q. You, I. Y. Zhang, X. Zhang, Y. Zhao, B. R. Brooks, G. K. L. Chan, D. M. Chipman, C. J. Cramer, W. A. Goddard, M. S. Gordon, W. J. Hehre, A. Klamt, H. F. Schaefer, M. W. Schmidt, C. D. Sherrill, D. G. Truhlar, A. Warshel, X. Xu, A. Aspuru-Guzik, R. Baer, A. T. Bell, N. A. Besley, J.-D. Chai, A. Dreuw, B. D. Dunietz, T. R. Furlani, S. R. Gwaltney, C.-P. Hsu, Y. Jung, J. Kong, D. S. Lambrecht, W. Liang, C. Ochsenfeld, V. A. Rassolov, L. V. Slipchenko, J. E. Subotnik, T. Van Voorhis, J. M. Herbert, A. I. Krylov, P. M. W. Gill and M. Head-Gordon, *Mol. Phys.*, 2015, **113**, 184–215.

34 J. P. Perdew, K. Burke and M. Ernzerhof, *Phys. Rev. Lett.*, 1996, **77**, 3865–3868.

35 S. Grimme, *J. Comput. Chem.*, 2006, **27**, 1787–1799.

36 Q. Wu and T. Van Voorhis, *Phys. Rev. A*, 2005, **72**, 024502.

37 L. F. Pacios, *J. Comput. Chem.*, 1995, **16**, 133–145.

38 G. Kresse and J. Furthmüller, *Comput. Mater. Sci.*, 1996, **6**, 15–50.

39 G. Kresse and J. Furthmüller, *Phys. Rev. B: Condens. Matter Mater. Phys.*, 1996, **54**, 11169–11186.

40 G. Kresse and J. Hafner, *Phys. Rev. B: Condens. Matter Mater. Phys.*, 1993, **47**, 558–561.

41 P. Lazar, F. Karlický, P. Jurečka, M. Kocman, E. Otyepková, K. Šafářová and M. Otyepka, *J. Am. Chem. Soc.*, 2013, **135**, 6372–6377.

42 K. M. Bal and E. C. Neyts, *Phys. Chem. Chem. Phys.*, 2018, **20**, 8456–8459.

43 B. Kaduk, T. Kowalczyk and T. Van Voorhis, *Chem. Rev.*, 2012, **112**, 321–370.

44 K. Leung, *J. Phys. Chem. C*, 2013, **117**, 1539–1547.

45 K. Leung, Y. Qi, K. R. Zavadil, Y. S. Jung, A. C. Dillon, A. S. Cavanagh, S.-H. Lee and S. M. George, *J. Am. Chem. Soc.*, 2011, **133**, 14741–14754.

46 H. Oberhofer and J. Blumberger, *J. Chem. Phys.*, 2009, **131**, 064101.

47 H. Oberhofer, K. Reuter and J. Blumberger, *Chem. Rev.*, 2017, **117**, 10319–10357.

48 C. O. Laoire, E. Plichta, M. Hendrickson, S. Mukerjee and K. M. Abraham, *Electrochim. Acta*, 2009, **54**, 6560–6564.

49 N. L. Ritzert, J. Rodríguez-López, C. Tan and H. D. Abruña, *Langmuir*, 2013, **29**, 1683–1694.

50 D. Astruc, *Eur. J. Inorg. Chem.*, 2017, **2017**, 6–29.

51 A. M. Bond, E. A. McLennan, R. S. Stojanovic and F. G. Thomas, *Anal. Chem.*, 1987, **59**, 2853–2860.

52 A. S. Cuharuc, G. Zhang and P. R. Unwin, *Phys. Chem. Chem. Phys.*, 2016, **18**, 4966–4977.

53 W. Li, C. Tan, M. A. Lowe, H. D. Abruña and D. C. Ralph, *ACS Nano*, 2011, **5**, 2264–2270.

54 J.-H. Zhong, J. Zhang, X. Jin, J.-Y. Liu, Q. Li, M.-H. Li, W. Cai, D.-Y. Wu, D. Zhan and B. Ren, *J. Am. Chem. Soc.*, 2014, **136**, 16609–16617.

55 M. M. Lucchese, F. Stavale, E. H. M. Ferreira, C. Vilani, M. V. O. Moutinho, R. B. Capaz, C. A. Achete and A. Jorio, *Carbon*, 2010, **48**, 1592–1597.

56 A. S. Danis, M. J. Counihan, K. O. Hatfield, J. Zhang, G. Agarwal, L. Zhang, R. S. Assary and J. Rodríguez-López, *Electrochim. Acta*, 2023, **447**, 142123.

57 J. V. Macpherson, *Phys. Chem. Chem. Phys.*, 2015, **17**, 2935–2949.

58 V. Mortet, A. Taylor, Z. Vlčková Živcová, D. Machon, O. Frank, P. Hubík, D. Tremouilles and L. Kavan, *Diamond Relat. Mater.*, 2018, **88**, 163–166.

59 V. Mortet, Z. Vlčková Živcová, A. Taylor, O. Frank, P. Hubík, D. Trémouilles, F. Jomard, J. Barjon and L. Kavan, *Carbon*, 2017, **115**, 279–284.

60 C. E. D. Chidsey, *Science*, 1991, **251**, 919–922.

61 H. O. Finklea, K. Yoon, E. Chamberlain, J. Allen and R. Haddox, *J. Phys. Chem. B*, 2001, **105**, 3088–3092.

62 S. Gosavi and R. A. Marcus, *J. Phys. Chem. B*, 2000, **104**, 2067–2072.

63 N. Holmberg and K. Laasonen, *J. Chem. Theory Comput.*, 2017, **13**, 587–601.

64 C. S. Sevov, S. K. Samaroo and M. S. Sanford, *Adv. Energy Mater.*, 2017, **7**, 1602027.

65 W. Duan, J. Huang, J. A. Kowalski, I. A. Shkrob, M. Vijayakumar, E. Walter, B. Pan, Z. Yang, J. D. Milshtein, B. Li, C. Liao, Z. Zhang, W. Wang, J. Liu, J. S. Moore, F. R. Brushett, L. Zhang and X. Wei, *ACS Energy Lett.*, 2017, **2**, 1156–1161.

10110 | *J. Mater. Chem. A*, 2025, **13**, 10097–10110

This journal is © The Royal Society of Chemistry 2025